Pore Size Determination of MCM-41 Mesoporous Materials by means of ¹H NMR Spectroscopy, N₂ adsorption, and HREM. A Preliminary Study

Ralf Schmidt,* Eddy Walther Hansen, Michael Stöcker, Duncan Akporiaye, and Ole Henrik Ellestad

Contribution from SINTEF, P.O. Box 124, Blindern, N-0314 Oslo, Norway

Received October 3, 1994®

Abstract: The aim of the present study is to derive a mathematical pore size distribution function containing a limited number of adjustable parameters. These parameters can be determined exclusively from ¹H NMR measurements. Regular mesoporous MCM-41 materials with different pore sizes, ranging from 20 to 30 Å, were synthesized and characterized by HREM, N₂ adsorption, and ¹H NMR. The pore sizes determined by N₂ adsorption and HREM were in good agreement. The ¹H NMR technique was used to determine the freezing point of water enclosed in water-saturated samples. By combining N₂ adsorption and ¹H NMR measurements, a simple relation was found between the freezing point depression (ΔT) and the pore radius (R_p): $\Delta T = K/(R_p - t_f)$ with $t_f = 3.49 \pm 0 36$ Å. The observation that $t_f \neq 0$ is tentatively explained by the formation of a surface layer of nonfreezing water of thickness t_f, which effectively reduces the actual pore radius from R_p to $R_p - t_f$. A mathematical model is derived which enables the pore size distribution to be determined from ¹H NMR intensity vs temperature measurements of water-saturated materials. The pore size distribution of amorphous silica determined independently by ¹H NMR and N₂ adsorption agreed well. However, the pore size of a microporous VPI-5 material ($R_p = 6.05$ Å) could not be predicted by the present model.

Introduction

It is well known that the microgeometry of porous media plays an important role in the physical and chemical properties of porous materials. For example, pore size, pore connectivity, fluid flow, and other transport processes in the pores are important in catalysis and permeation in rocks and of major concern for the oil and process industry (EOR). The classical model used in determining pore sizes are gas adsorption—desorption techniques[1] and mercury porosimetry.[2] Both of these methods are quite time consuming. Moreover, mercury porosimetry is a destructive technique, resulting in an irreversible damage of the investigated material.

Much effort has been devoted to NMR relaxation time data (T_1 and T_2) to infer pore size distribution in rocks. Some relevant articles covering these topics can be found in the list of references.[3-12] Alnaimi et al.[13] investigated the melting point of different liquids (e.g., cyclohexane) confined in porous

predried silica with pores in the range 60—1000 Å by measuring the NMR signal as a function of temperature. However, their samples did not cover the range of mesopores below 60 Å, which is an important region in catalysis. Moreover, it is well known that the pore characteristics of their samples are rather complex due to irregularities and interconnections of pores of the host material, e.g., amorphous silica.

Recently, the synthesis of a new family of mesoporous materials, with regular ordered pores, denoted as M41S materials was reported.[14,15] One member of this family, MCM-41, possesses a hexagonal array of uniform, regular, one-dimensional pores and has already initiated considerable industrial and academic interest.[16,17] The pore size of these materials can be systematically varied in the range of 18 to 100 Å by changing the synthesis conditions. Due to their geometric regularity, these

* To whom correspondence should be addressed.
® Abstract published in *Advance ACS Abstracts,* March 15, 1995.
(1) Sing, K. S. W.; Everett, D. H.; Haul, R. A. W.; Moscou, L.; Pierotti, R. A.; Rouquérol, J.; Siemieniewska, T. *Pure Appl. Chem.* **1985,** *57,* 603—619.
(2) Gregg, S. J.; Sing, K. S. W. *Adsorption, Surface Area and Porosity,* 2nd ed.; Academic Press: New York, 1982; pp 173—190.
(3) D'Orazio, F.; Tarczon, J. C.; Halperin, W. P.; Eguchi, K.; Mizusaki, T. *J. Appl. Phys.* **1989,** *65,* 742—751.
(4) Lahajnar, G.; Blinc, R.; Rutar, V.; Smole, V.; Zupancic, I.; Kocuvan, I.; Ursic, J. *Cem. Concr. Res.* **1977,** *7,* 385—394.
(5) Brown, R. J. S.; Fatt, I. *Trans. AIME* **1956,** *207,* 262—264.
(6) Howard, J. J.; Kenyon, W. E. *Marine Petrol. Geol.* **1992,** *9,* 139—145.
(7) Kenyon, W. E. *Nucl. Geophys.* **1992,** *6,* 153—171.
(8) Salanthiel, R. A. *J. Petrol. Tech.* **1973,** *20,* 1973.
(9) Link, J.; Kaufmann, J.; Schenker, K. *Magn. Reson. Imaging* **1994,** *12,* 203—205.
(10) Mendelson, J. S. *J. Appl. Phys.* **1982,** *53,* 6465—6466.
(11) Pabitra, N. S.; Schwartz, L. M.; Partha, P. M. *Magn. Reson. Imaging* **1995,** *12,* 227—230.
(12) Kleinberg, R. L. *Nature* **1994,** *351,* 467—468.

(13) Alnami, S. M.; Strange, J. H.; Smith, E. G. *Magn. Reson. Imaging* **1994,** *12,* 257—259.
(14) Kresge, C. T.; Leonowicz, M. E.; Roth, W. J.; Vartuli, J. C.; Beck, J. S. *Nature* **1992,** *359,* 710—713.
(15) Beck, J. S.; Vartuli, J. C.; Roth, W. J.; Leonowicz, M. E.; Kresge, C. T.; Schmitt, K. D.; Chu, C. T.-U.; Olsen, D. H.; Sheppard, E. W.; McCullen, S. B.; Higgins, J. B.; Schlenker, J. L. *J. Am. Chem. Soc.* **1992,** *114,* 10834—10843.
(16) (a) Beck, J. S. U.S. Patent no. 5057296, 1991. (b) Kresge, C. T.; Leonowicz, M. E.; Roth, W. J.; Vartuli, J. C. U.S. Patent no. 5098684, 1992, and U.S. Patent no. 5102643, 1992. (c) Beck, J. S.; Chu, C. T.-U.; Johnson, I. D.; Kresge, C. T.; Leonowicz, M. E.; Roth, W. J.; Vartuli, J. C. U.S. Patent no. 5108725, 1992.
(17) (a) Chen, C.-Y.; Burkett, S. L.; Li, H.-X.; Davis, M. E. *Microporous Mater.* **1993,** *2,* 27—34. (b) Alfredsson, V.; Keung, M.; Monnier, A.; Stucky, G. D.; Unger, K. K.; Schüth, F. *J. Chem. Soc., Chem. Commun.* **1994,** 921. (c) Corma, A.; Fornés, V.; Navarro, M. T.; Pérez-Pariente, J. *J. Catal.* **1994,** *148,* 569—574. (d) Huo, Q.; Margolese, D. I.; Ciesla, U.; Feng, P.; Gier, T. E.; Sieger, P.; Leon, R.; Petroff, P. M.; Schüth, F.; Stucky, G. D. *Nature* **1994,** *368,* 317—321. (e) Feuston, B. P.; Higgins, J. B. *J. Phys. Chem.* **1994,** *98,* 4459—4462. (f) Steel, A.; Carr, S. W.; Anderson, M. W. *J. Chem. Soc., Chem. Commun.* **1994,** 1571. (g) Monnier, A.; Schüth, F.; Huo, Q.; Kumar, D.; Margolese, D.; Maxwell, R. S.; Stucky, G. D.; Krishnamurty, M.; Petroff, P.; Firouzi, A.; Janicke, M.; Chmelka, B. F. *Science* **1993,** *261,* 1299—1303.

materials represent ideal model systems[18,19] and have therefore been used in the present study.

Using ^{1}H NMR, the effect of pore size on the freezing/melting transition of water confined in porous materials has been investigated.[13,20-22] ^{1}H NMR intensity vs temperature data (referred to as IT data or IT curves) of water confined in MCM-41 materials with varying pore sizes will be presented. By comparing these NMR results with N_2 adsorption and HREM studies (on the same materials), a correlation between pore size and freezing point depression of frozen pore water is established. A mathematical model is derived which determines the pore size distribution from observed ^{1}H NMR IT curves. This model is applied to a crystalline microporous material (VPI-5) and a mesoporous amorphous silica.

Experimental Section

Materials. The different MCM-41 materials were prepared according to synthesis procedures similar to those reported by Beck et al.[15]

I. Sample 1. A quantity of 7.8 g of sodium silicate (Kebo, 8.9% Na_2O, 28% SiO_2) was added to a well-mixed solution of 50 g of distilled water and 0.3 g of sulfuric acid (Merck, 95%) under stirring. After the formed gel was stirred for 10 min, the pH of the gel was adjusted to pH = 12 by addition of a NaOH solution. Then 83.75 g of a template/water mixture (21 g of $C_{16}H_{33}(CH_3)_3NCl$ in 62.75 g of distilled water) was added. The formed gel was stirred for about 0.5 h before 20 g of distilled water was added. The molar composition of the gel was $SiO_2:C_{16}H_{33}(CH_3)_3NCl:H_2O$ = 1:1.8:180, respectively. The gel was loaded into a stoppered Teflon bottle and heated without stirring at 100 °C for 24 h. After cooling to room temperature, the resulting solid product was recovered by filtration, extensively washed with distilled water, and dried in air at ambient temperature.

II. Samples 2 and 3. A quantity of 40 g of distilled water, 1.2 g of sulfuric acid (Merck, 95%), and 18.7 g of sodium silicate (Kebo, 8.9% Na_2O, 28% SiO_2) were mixed, and the resulting gel was stirred intensively for 10 min (sample 2) and 20 min (sample 3). Then the template solution (15.5 g of $C_{14}H_{29}(CH_3)_NBr$ (Aldrich, 99%) in 46.5 g distilled water) was added, and the formed gel was subsequently stirred for about 0.5 h before 20 g of distilled water was added. The molar composition of the different gels was $SiO_2:C_{14}H_{29}(CH_3)_3NBr:H_2O$ = 10:5:825. The respective gels were loaded into stoppered Teflon bottles, heated without stirring at 100 °C for 144 h, and processed as described above. The template of samples 1−3 was removed by calcination at 813 K for 1 h in flowing nitrogen followed by 6 h in flowing air with flow rates of 100 mL/min.

The VPI-5 material used was synthesized according to Davis et al.,[23] and the amorphous silica was purchased from Merck (kieselgel 60).

Characterization/Analysis. The solid materials were characterized by X-ray powder diffraction (Siemens D5000 diffractometer with a germanium monochromator, Cu Kα radiation), and high-resolution electron microscopy (HREM) using a JEOL 2000 FX instrument equipped with a fiber optic coupled GATAN 622 TV-system. The TEM instrument was operated at 200 kV using spot size 3 and primary magnifications between 50000× and 100000×. The samples were prepared by crushing the material in ethanol and dropping the finely ground material onto a holey carbon film.

(18) (a) Franke, O.; Schulz-Ekloff, G.; Rathousky, J.; Starek, J.; Zunkal, A. *J. Chem. Soc., Chem. Commun.* **1993**, 724. (b) Branton, P. J.; Hall, P. G.; Sing, K. S. W. *J. Chem. Soc., Chem. Commun.* **1993**, 1257. (c) Llewellyn, P. L.; Grillet, Y.; Schüth, F.; Reichert, H.; Unger, K. K. *Microporous Mater.* **1994**, *3*, 345−349.

(19) Akporiaye, D.; Hansen, E. W.; Schmidt, R.; Stöcker, M. *J. Phys. Chem.* **1994**, *98*, 1926−1928.

(20) Strange, J. H.; Rahman, M.; Smith, E. G. *Phys. Rev. Lett.* **1993**, *71*, 3589−3591.

(21) Pearson, R. T.; Derbyshire, W. *J. Colloid Interface Sci.* **1974**, *46*, 232−248.

(22) (a) Overloop, K.; Van Gerven, L. *J. Magn. Reson. Ser. A* **1993**, *101*, 147−156. (b) Overloop, K.; Van Gerven, L. *J. Magn. Reson. Ser. A* **1993**, *101*, 179−187.

(23) Davis, M. E.; Montes, C.; Garces, J. M. *ACS Symp. Ser.* **1989**, *398*, 291−304.

N_2 Adsorption/Desorption. Nitrogen adsorption−desorption isotherms were measured at 77 K with a Carlo Erba instrument using a conventional volumetric technique. The samples were outgassed at 150 °C for 1 h, and the mean pore size was calculated using the Kelvin equation:[24]

$$R_K = \frac{2\sigma^{lg}V^l}{RT \ln\left(\frac{p_0}{p}\right)} = \frac{K_{ads}}{\ln\left(\frac{p_0}{p}\right)} \qquad (1)$$

This relates the Kelvin radius R_K to the relative pressure p/p_0, at which pore condensation of the adsorbate occurs; σ^{lg} is the surface tension of the liquid condensate and V^l the molar volume. R represents the universal gas constant at the absolute temperature T. K_{ads} was determined to be 9.4 Å.[25] If one assumes cylindrical pores with radius R_p and zero contact angle, R_p is related to the Kelvin radius via eq 2

$$R_p = R_K + t_{ads} \qquad (2)$$

where t_{ads} represents a correction term for the thickness of the initially adsorbed layer on the pore surface. From tabulated values of R_K and t_{ads},[25] a linear function between R_p and R_K was found;

$$R_K = \alpha R_p + \beta \qquad (3)$$

with $\alpha = 0.9187 \pm 0.0014$ and $\beta = -4.393 \pm 0.076$. The correlation coefficient of the fit was 0.999939 with a standard error of estimate better than 0.20 Å for $R_p > 11$ Å. The N_2 adsorption−desorption curves relate the volume of N_2 to the relative pressure p/p_0. In order to determine pore size distribution, an expression dV/dR_p vs R_p is needed. Such an expression can easily be derived by noting that

$$\frac{dV}{dR_p} = \frac{dV}{d\left(\frac{p}{p_0}\right)} \frac{d\left(\frac{p}{p_0}\right)}{dR_K} \frac{dR_K}{dR_p} \qquad (4)$$

The first term on the right side of eq 4 is determined by numerical derivation of the adsorption−desorption isotherm with respect to p/p_0. The other two terms in eq 4 can be expressed by p/p_0 by combining eqs 1 and 3, giving

$$\frac{dV}{dR_p} = 2.356 \frac{dV}{d\left(\frac{p}{p_0}\right)} \left[\ln^2\left(\frac{p_0}{p}\right)\right] \frac{p}{p_0} \qquad (5)$$

Thus, a plot of dV/dR_p vs R_p can be established.

^{1}H NMR. The water-saturated samples were studied by ^{1}H NMR in the temperature range 273−183 K using a Varian VXR 300 S NMR spectrometer operating at 300 MHz proton resonance frequency. The accuracy of the temperature determination was within ±0.5 K. A bandwidth of 100 kHz and an acquisition time of 0.050 s were applied with a repetition time of 10 s between rf pulses to ensure quantitative sampling of the NMR signal. The long interpulse timing was imposed by the long spin−lattice relaxation time of the silanol protons which exhibited spin−lattice relaxation times of approximately 2−3 s. All measurements were performed with a 90° pulse of 16 μs. Each spectrum was composed of 16 transients. The sample was temperature equilibrated for 5 min at each temperature before any measurements were performed. The intensities were determined by numerical integration of the peaks and were corrected for temperature according to Curie's law, i.e., the NMR signal intensity measured at an absolute temperature T was corrected by multiplication by the factor T/T_0, with $T_0 = 273.15$ K.

Since the intensity of the pore water is the key parameter of these NMR measurements, it is of utmost importance that the interparticular water has frozen completely at 0 °C. However, preliminary observations showed that this surface water did not freeze above −5 °C, even

(24) Thompson, W. *Philos. Mag.* **1871**, *42*, 448.

(25) Gregg, S. J.; Sing, K. S. W. *Adsorption, Surface Area and Porosity*, 2nd ed.; Academic Press, New York, 1982; pp 132−152.
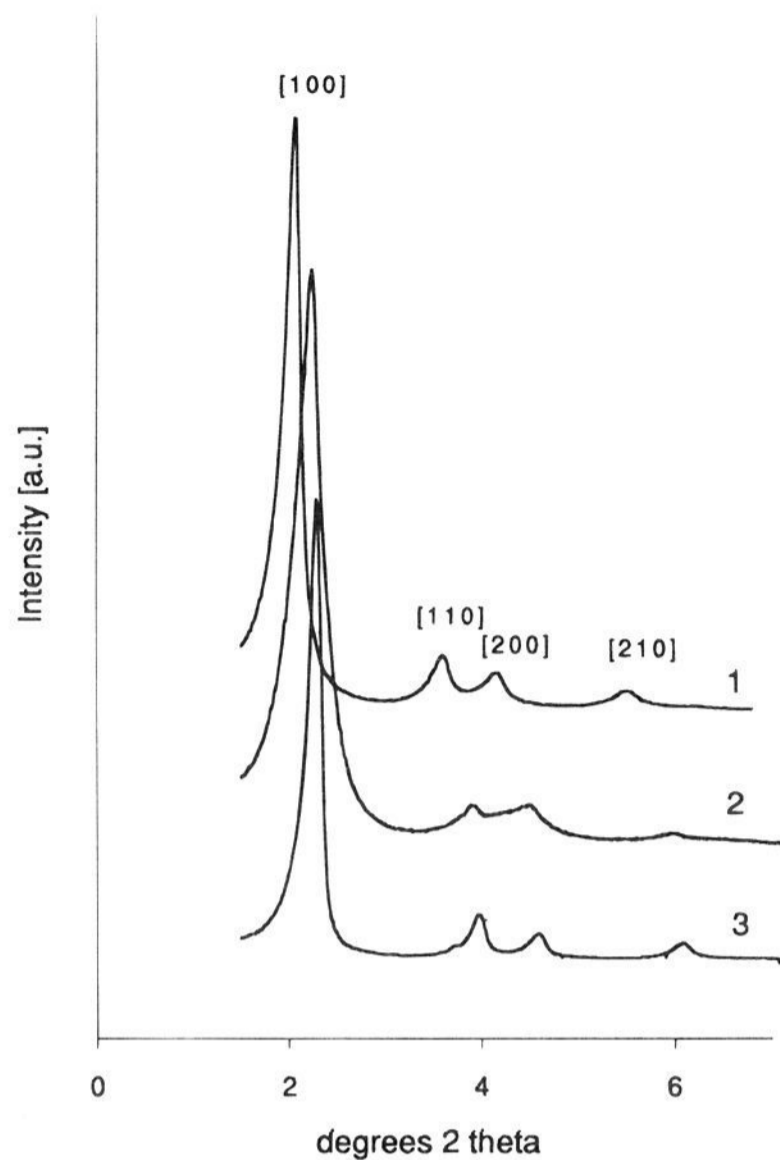
Figure 1. X-ray powder diffraction patterns of samples 1, 2, and 3.

Table 1. Characterization Data of the Different MCM-41 Materials

	d value [100] [Å]		N_2 BET	pore
sample	as-synthesized	calcined	surface $[m^2/g]$	volume $[cm^3/g]$
1	43	35	1175	1.12
2	39	31.5	1178	1.03
3	38	28.5	1200	0.87

after 5 h of temperature equilibration at this temperature. Nor did bulk water confined in the 5 mm NMR tube freeze at this temperature. The temperature had to be lowered to about −12 °C before spontaneous freezing of bulk water took place. Thus, the following procedure was used throughout this work: The sample was cooled to −15 °C for 10 min and then warmed to −1 °C before the cooling experiment was initiated. This procedure ensured that all surface and bulk water was frozen out before the actual recording of the NMR spectra was started. The ^1H NMR IT curve was obtained by gradually cooling the sample to 191 K and then heating the sample to 273 K while recording the different spectra.

Results

The X-ray diffractograms of the as-synthesized samples 1−3 are shown in Figure 1. For all three samples, four low-angle peaks can clearly be resolved and are indexed according to a hexagonal unit cell.[15] The d_{100} values of as-synthesized and calcined MCM-41 samples, the BET surface area, and the pore volumes (determined by N_2 adsorption) are summarized in Table 1. A decrease of about 8 Å in the d_{100} values upon calcination was observed for samples 1 and 2, which agrees well with the values reported by Chen et al.[26] for comparable samples. Sample 3 showed a somewhat larger decrease of 9.5 Å in the d_{100} value. The one-dimensional pore structure of the materials

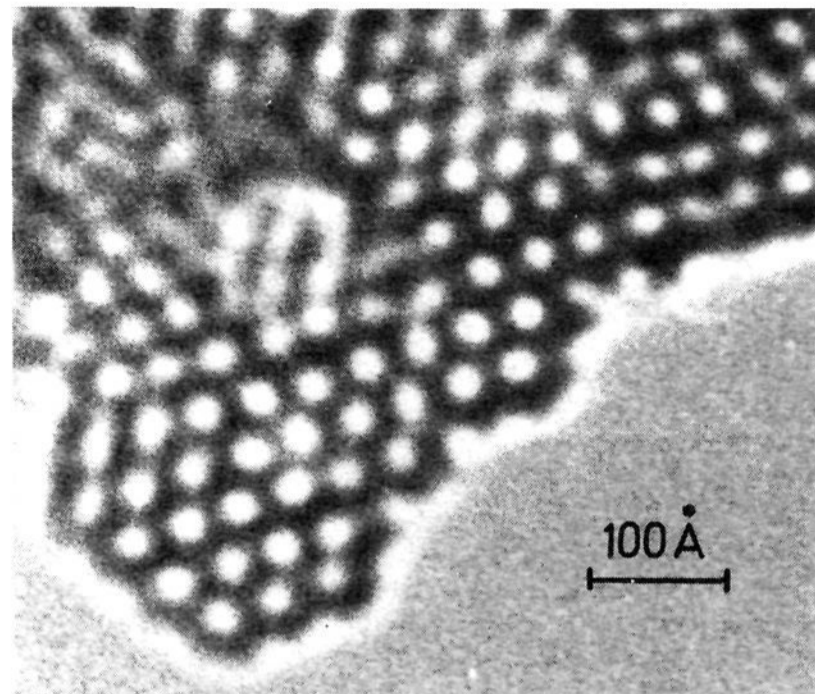(26) Chen, C.-Y.; Li, H.-X.; Davis, M. E. *Microporous Mater.* **1993**, *2*, 17.

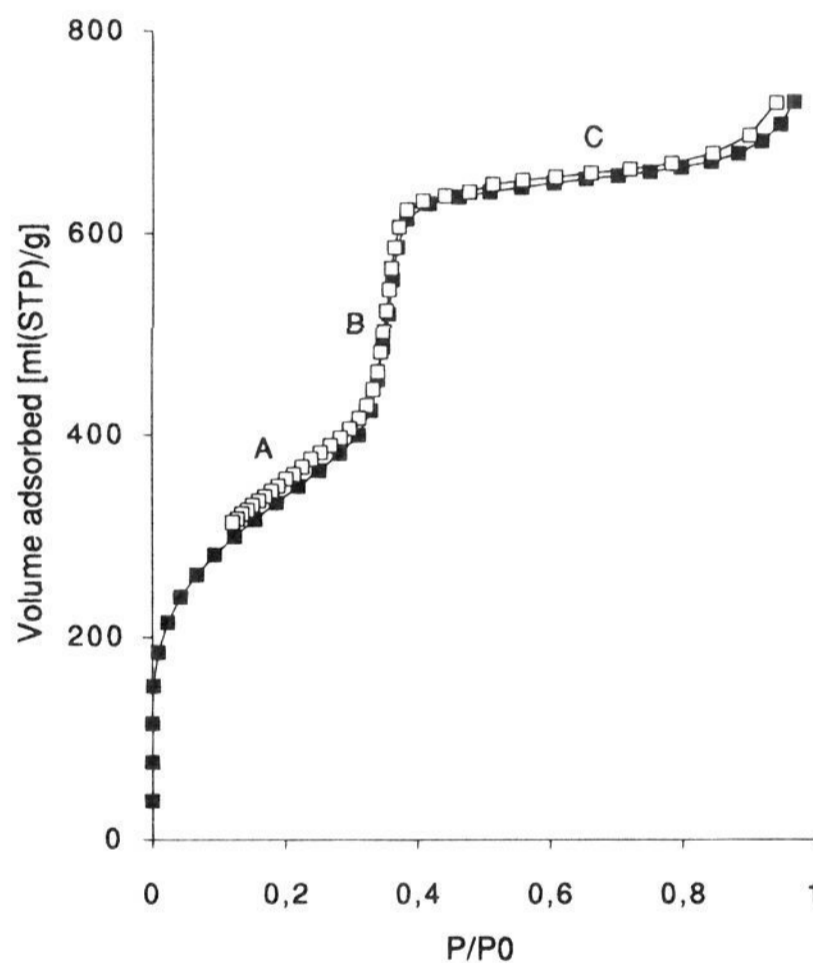**Figure 2.** High-resolution electron micrograph of the pore structure of sample 1.

Figure 3. Nitrogen adsorption isotherm of sample 1 at 77 K (adsorption ■, desorption □).

was confirmed by HREM investigations. In Figure 2, an HREM micrograph of the hexagonal ordered pores of sample 1 is shown. The dark areas represent pore walls and the white areas the actual pores. Also, one-dimensional regularly ordered pores are observed for samples 2 and 3. The N_2 adsorption isotherm of sample 1 is shown in Figure 3. Three well-distinguished regions of the adsorption isotherm can be noticed: a linear increase of the adsorbed volume at low pressure due to monolayer−multilayer adsorption on the pore walls (A), a sharp increase in the adsorbed volume at intermediate pressure due to capillary condensation (B), and a subsequent linear increase in the adsorbed volume vs pressure at high pressure due to multilayer adsorption on the outer surface (C).

The N_2 adsorption isotherms of samples 1 to 3 are shown in Figure 4. For all three samples, no hysteresis in the adsorption−desorption isotherms were observed, which is in agreement with the N_2 isotherms reported for different MCM-41 materials with comparable pore sizes.[18,26] The sharp increase in the adsorbed
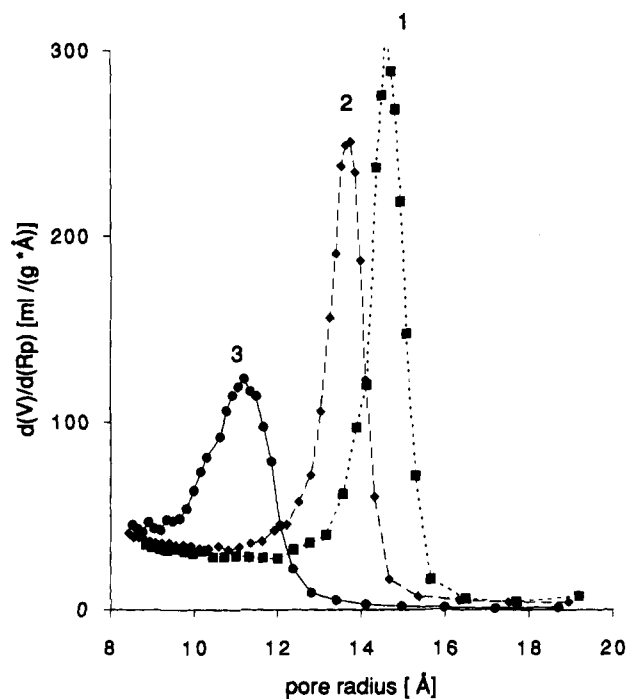
4052 *J. Am. Chem. Soc., Vol. 117, No. 14, 1995*

Schmidt et al.
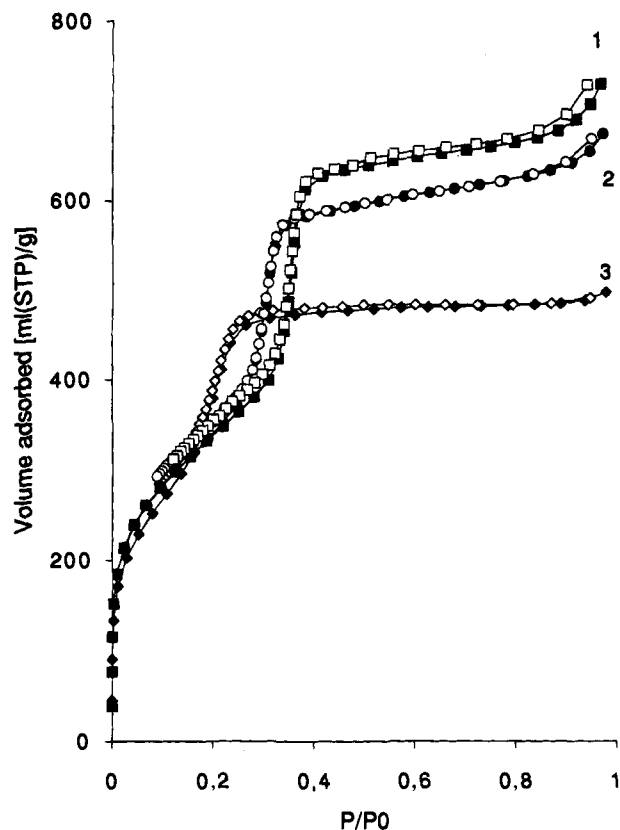
Figure 4. Nitrogen adsorption isotherms of samples 1, 2, and 3. Filled symbols denote adsorption, open symbols denote desorption.

Figure 5. Pore size distributions of samples 1, 2, and 3 calculated from N_2 adsorption.

Figure 6. ^1H NMR spectra of water enclosed in the pores of sample 1 as a function of temperature.

volume of N_2 due to capillary condensation occurs at different relative pressures, p/p_0, for the three samples investigated. The range of relative pressure at which pore condensation occurs, the relative pressure at the inflection point, the pore radius R_K (determined by N_2 adsorption, eq 1), and the monolayer thickness t_{ads} are summarized in Table 2.
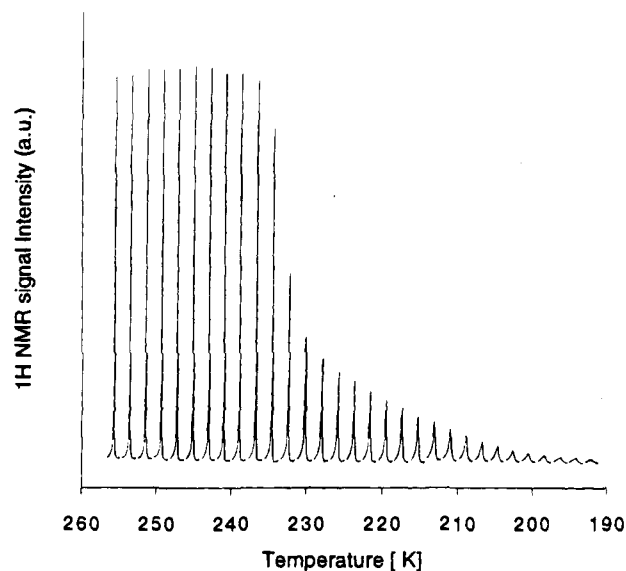
Additionally, the range of pore radii, determined by HREM investigations, is included in Table 2. The VPI-5 material had a surface area of 210 m^2/g, determined by one-point BET analysis.

The pore size distributions (dV/dR_p vs R_p) of the different MCM-41 materials were calculated from the N_2 adsorption data (eq 5) assuming cylindrical pores and are shown in Figure 5. Samples 1 and 2 show quite narrow pore size distributions centered around 14.6 and 13.4 Å, respectively, with a half-width of about 0.8 Å (Gaussian fit). Sample 3, however, shows a significantly broader distribution with a half-width of approximately 1.2 Å (Gaussian fit) and an average pore radius of 11.2 Å.

The ^1H NMR spectra of confined pore water vs temperature (from 258 to 193 K) of sample 1 are illustrated in Figure 6 and show clearly that the intensity decreases and the line width increases with decreasing temperature due to freezing of pore water. A sharp transition of the ^1H NMR signal intensity at approximately 230 K can be observed, corresponding to the freezing of pore water.[19,22] The broader transition observed below 230 K is not attributed to a normal colligative freezing

of pore water and is discussed extensively by Overloop et al.[21,22] This subject is rather complex and will not be discussed any further in this work. The ^1H NMR IT curves obtained after multiple cooling/heating cycles of sample 1 are shown in Figure 7 and are within experimental error identical. Upon warming the samples from 191 to 273 K, the IT curves revealed a small hysteresis effect of approximately 3 K for all three cooling/ warming cycles investigated. Sample 2 and sample 3, however, showed no such effects. The IT curves (after cooling to 191 K) of the three MCM-41 samples and the VPI-5 material are

Table 2. Pore Size Characterization Data of the Studied MCM-41 Materials

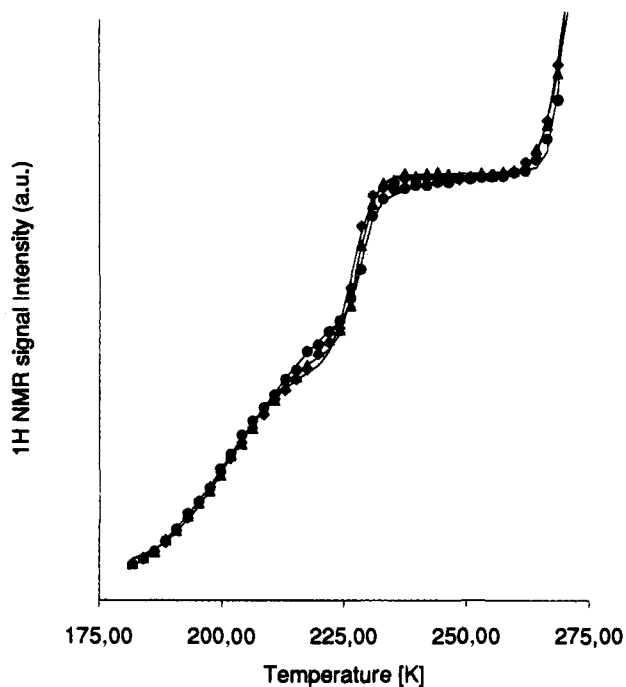| samples	rel pressure range (P/P_0)	P/P_0 at inflection point	t_{ads} [Å]	pore radius (R_p) from N_2 [Å]	pore radius (R_p) determined by HREM [Å]
1	0.32−0.38	0.35	5.4	14.6	15 ± 2
2	0.28−0.33	0.31	5.1	13.4	14 ± 2
3	0.18−0.26	0.23	4.6	11.2	11 ± 2

Figure 7. ^{1}H NMR signal intensity of water enclosed in the pores of sample 1 as a function of temperature, after 1 (◆), 2 (▲), and 3 (●) cooling/heating cycles.
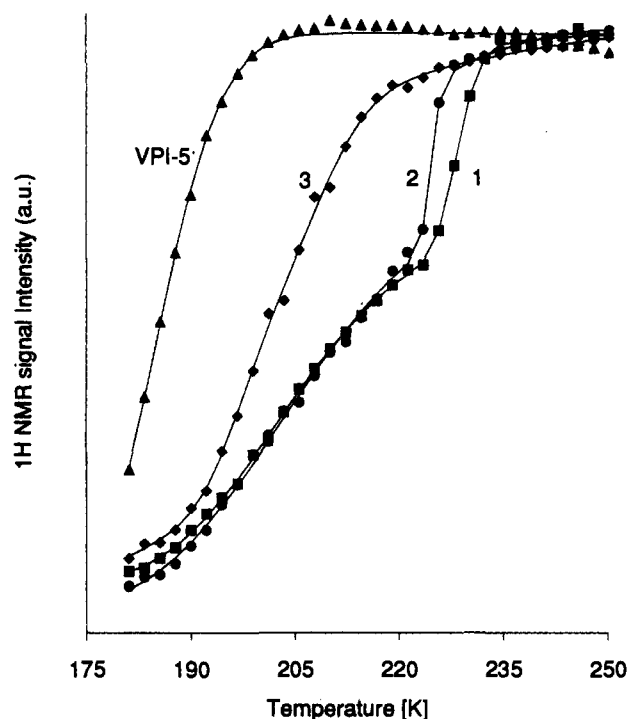

Figure 8. ^{1}H NMR signal intensity of water enclosed in the pores of samples 1, 2, and 3 and of a crystalline VPI-5 sample as a function of temperature.

shown in Figure 8 and signify a transition temperature in all the samples. A significantly lower transition temperature of water confined in VPI-5 compared to the MCM-41 materials can be observed. The solid lines in Figure 8 represent model calculations. This model has been derived in a recent publication[19] and has the following generalized form:

$$I(X) = \sum_{i=1}^{N} \frac{I_{0i}}{\sqrt{\pi}} \int_0^{(X-X_{ci})/\sqrt{2}\Delta_i} \exp(-u^2)\,du \qquad (6)$$

Table 3. Values of the Analytical Fit of the ^{1}H NMR vs Temperature Curves

	sample 1	sample 2	sample 3
T_{ci}	4.379 ± 0.0018	4.499 ± 0.013	4.779 ± 0.076
Δ_i	0.047 ± 0.0031	0.046 ± 0.021	0.119 ± 0.046

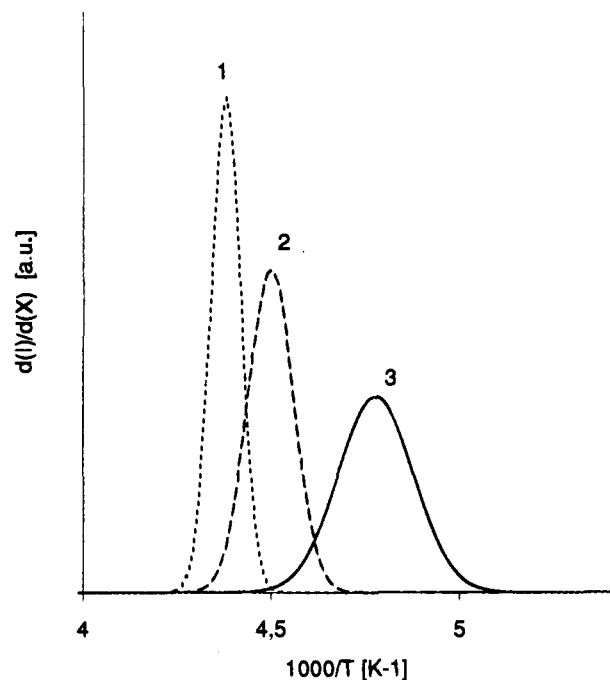**Figure 9.** Distribution of the change of ^{1}H NMR signal intensity per change in the inverse temperature X (= 1000/T) as a function of the inverse temperature X.

where $I(X)$ represents the amount of mobile pore water at the inverse temperature X (= 1000/T), I_{0i} is the amount of confined pore water, T_{ci} (= 1000/T_{ci}) represents the phase transition temperature, and Δ_i is the width of the transition curve. For a sharp transition, Δ_i approaches zero. By differentiating eq 6 with respect to X we obtain:

$$\frac{dI}{dX} = \sum_{i=1}^{N} \frac{I_{0i}}{\sqrt{\pi}} \exp\left(-\left|\frac{X - X_{ci}}{\sqrt{2}\Delta_i}\right|^2\right) \qquad (7)$$

showing that dI/dX is described by a sum of Gaussian functions. The transition temperature X_{ci} = (1000/T_{ci}), the width Δ_i, and the fraction I_{ci} are determined by fitting eq 6 to the observed intensity $I(X)$ by a nonlinear least-squares fit. The results are summarized in Table 3. The inverse temperature distribution curves dI/dX vs X for the three MCM-41 materials are presented in Figure 9 and illustrate that the width of the distribution curves are somewhat larger for sample 3 than samples 1−2.

By combining ^{1}H NMR data (Figure 9, Table 3) and N$_2$ adsorption data (Figure 5, Table 2), the freezing point temperature depression ΔT (= $T_0 - T_c$) of the confined water can be plotted vs the inverse pore radius (1/R_p) in Figure 10. A model equation of the form

$$\Delta T = \frac{K_f}{R_p + t_f} \qquad (8)$$

is fitted to the experimental data, and the results are presented in Figure 10. The solid line was determined by fitting the parameters t_f and K_f by the nonlinear fit, resulting in K_f = 494.8 ± 19.6 K Å^{-1} and t_f = −3.49 ± 0.36 Å. The dotted line was
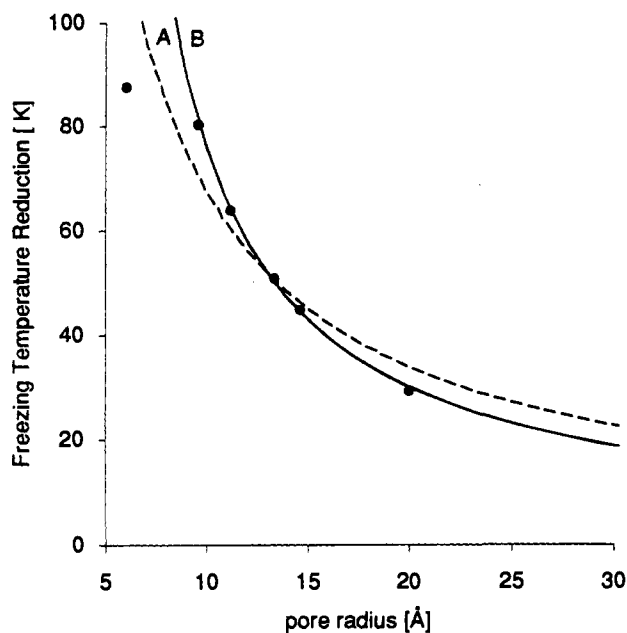
Figure 10. Pore radius (R_p), determined by N_2 adsorption vs freezing point depression (ΔT). The dotted line (A) represents the fit of the experimental data to $\Delta T = K_f/Rp$, and the solid line (B) the fit to $\Delta T = K_f/(Rp + t_f)$.
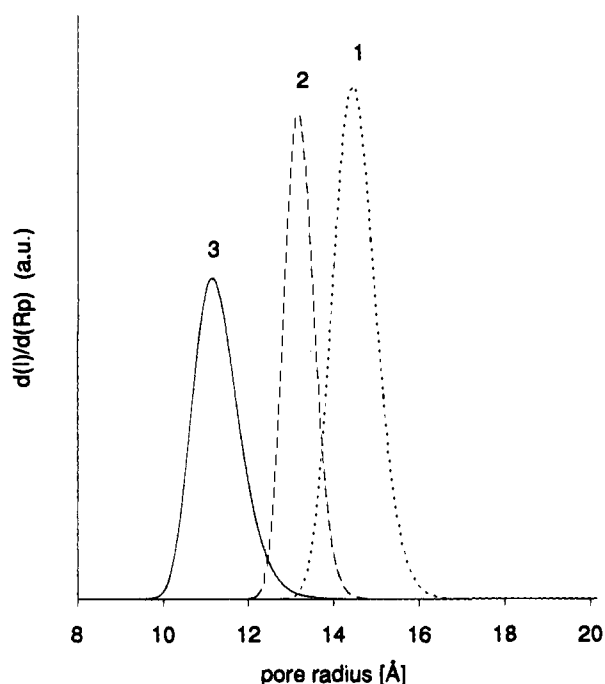
Figure 11. Pore size distributions of samples 1, 2, and 3 determined from ^1H NMR experiments.

determined by setting $t_f = 0$, resulting in $K_f = 676 \pm 24$ K $Å^{-1}$. In these fits, two further data points taken from a recent publication on MCM-41 materials[19] are included. These are $R_p = 20$ Å, $\Delta T = 29.3$ K and $R_p = 9.5$ Å, $\Delta T = 80$ K. The model equation (eq 8) implicitly assumes that $\Delta T = 0$ for $R_p = \infty$ which corresponds to the freezing point of bulk water $(R_p = \infty)$. The data point of well-crystallized alumino phosphate molecular sieves, VPI-5, with a pore radius of $R_p = 6.1$ Å[27] is also included in Figure 10. In Figure 11, the pore size distributions (dI/dR_p) of the three samples derived from the ^1H NMR IT experiments are presented. The calculation of dI/dRp from recorded ^1H NMR IT curves will be explained in detail in

(27) Davis, M. E.; Li, H. X. *Catal. Today* **1994**, *19*, 61–106.
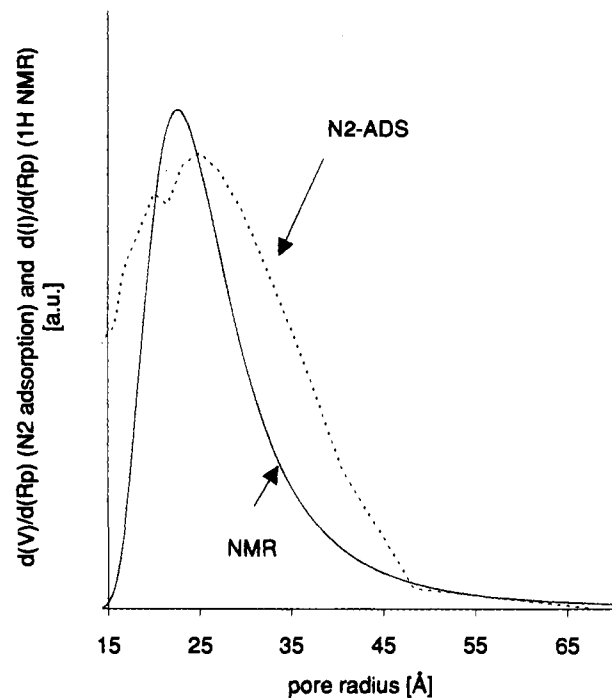
Figure 12. Pore size distribution of amorphous silica, calculated from nitrogen adsorption and ^1H NMR.

the Discussion section. For the determination of the pore size distribution of materials other than MCM-41, an amorphous silicate (kiesegel 60) was chosen. The results are shown in Figure 12 where the dotted curve represents the pore size distribution determined by N_2 adsorption, and the solid curve represents the pore size distribution determined by ^1H NMR. Both curves reveal quite broad pore distributions centered around 25 Å. However, the pore size distribution determined by N_2 adsorption is broader, in particular at larger pore sizes.

Discussion

The large pore volume (Table 1) and the fact that at least four low-angle peaks are resolved in the XRD diffractogram (Figure 1) indicate that high-quality MCM-41 materials were obtained. This is further supported by the HREM investigation (which shows a hexagonal ordering of the one-dimensional pores, Figure 2) and N_2 adsorption studies (Figures 3 and 4). The N_2 isotherms are typical for MCM-41 materials.[18] The increase of the adsorbed-N_2 volume, due to capillary condensation (region B, Figure 3), suggests significant pore volume of the one-dimensional cylindrical pores. The sharp increase in the adsorption isotherms observed at different relative pressures p/p_0 is due to the different pore sizes of the MCM-41 materials. Using a geometric model for the hexagonal honeycomb organization of the pores of the MCM-41 materials, the wall thickness (w) can be calculated by subtracting the pore diameter (determined by N_2 adsorption) from the unit cell size (a), which for a hexagonal symmetry is defined as $a = 2d_{100}/\sqrt{3}$. The wall thickness for samples 1, 2, and 3 were calculated to be 10, 8.5, and 11 Å, respectively, which agree well with the wall thicknesses reported for MCM-41 materials with comparable pore sizes.[15,26] The variation in the wall thickness may be due to slight differences in the synthesis procedure, which can have significant impact on the pore and unit cell size of the obtained material.[28] The larger reduction of the d_{100} value upon calcination and the broader pore size distribution of sample 3

(28) Coustel, N.; Di Renzo, F.; Fajula, F. *J. Chem. Soc., Commun.* **1994**, 1257.

compared to samples 1 and 2 may indicate that sample 3 might be less well crystallized compared to samples 1 and 2. This might also account for the smaller pore size of sample 3 compared to sample 2, even though very similar synthesis procedures were applied. However, as mentioned before, small variations in the synthesis procedure can have significant effects on the pore size. The pore size of about 30 Å reported by Chen et al.[26] for their material synthesized using $C_{16}H_{33}(CH_3)_3N^+$ as template agrees well with the pore size of the sample 1 (Table 2), which was synthesized using the same template. Beck et al.[15] report for their MCM-41 material using $C_{16}H_{33}(CH_3)_3N^+$ as template a pore size of 37 Å, which was determined by argon adsorption and Horvath−Kawazoe[29] analysis. This pore size would, however, result in an unrealistic wall thickness of 3 Å as the unit cell size was calculated to be 40 Å. This was explained by Beck et al.[15] to be most likely due to the precision of the pore size calculation based on the Horvath−Kawazoe model, which was originally developed for the calculation of microporous, layered carbons.[29] Beck et al.[15] further report for their MCM-41 material synthesized using a $C_{14}H_{29}(CH_3)_3N^+$ template a pore size of 30 Å, which is larger than the pore sizes determined for samples 2 and 3. This may be due to slight differences in the synthesis procedure or due to the precision of the pore size determination using the Horvath−Kawazoe method.

As illustrated in Figure 6, the transition temperature of the pore water in sample 1 can be clearly observed from the recorded ^1H NMR spectra vs temperature, suggesting ^1H NMR to be a sensitive technique in characterizing the freezing behavior of water confined in porous materials. As already pointed out in the Results section, the ^1H NMR IT curves were—within experimental error—identical for the three freezing/melting cycles (Figure 7), suggesting that the pore geometry (pore size) of the mesoporous materials are intact and not destroyed by any mechanical stress owing to the phase changes (ice ↔ water). The ^1H NMR IT curves (Figure 8) were fitted to a model equation (eq 6) which enabled a better estimate of the transition temperature, T_c, as well as the width, Δ_i, of the distribution curve. The model provides an excellent fit to the observed data points. The corresponding distribution of freezing points (or transition temperatures), dI/dX, are displayed in Figure 9. As can be seen from eq 7, the distribution function dI/dX vs X can be described as a sum of Gaussian functions which originates from the assumption of a log-normal distribution of correlation times of the confined water molecules.[22]

Gibbs and Thomas[24] related the freezing point depression, ΔT, of a liquid enclosed in a pore to the radius R_P of the pore by eq 9 which is in analogy with the relative pressure reduction of the condensation of a gas enclosed in a porous material (as described by eq 1, often referred to as Kelvin's law)

$$\Delta T = \frac{2\gamma T_c}{\varrho R_p \Delta H} = \frac{K_f}{R_p} \tag{9}$$

The results obtained on our MCM-41 model systems (Figure 10) show that the fit of eq 9 to the data is rather poor. However, by adding an adjustable parameter t_f to the denominator of eq 9 (see eq 8), a significant improvement in the fit was obtained. The parameter t_f was found to be negative (-3.49 Å). According to the early NMR work of Pearson et al.[21] and later Overloop et al.[22] on partially water-saturated and completely water-saturated amorphous silica, a nonfreezing layer of surface water with a thickness of one to three monomolecular layers of water was observed at low temperature. Taking into account a

(29) Horvath, G.; Kawazoe, K. *J. Chem. Eng. Jpn.* **1983**, *16*, 470.

95% confidence interval, the value of t_f can vary between 2 and 5 Å, corresponding to a thickness of one to two monomolecular layers of water. We tentatively believe that a nonfreezing layer of thickness t_f is formed on the pore surface which acts physically as part of the pore wall, resulting in a reduction of the effective pore radius from R_p to $R_p - t_f$. This interpretation explains the validity of eq 8 and is in analogy to the determination of the pore size by N_2 adsorption, where a multilayer thickness t_{ads} is introduced to calculate the pore size (eq 2).

At larger pore radii ($R_p \gg 3.49$ Å) the size of the nonfreezing surface layer (t_f) is much smaller than the pore radius, and eq 8 can be approximated by eq 9. It must also be emphasized that the VPI-5 material has a transition temperature which can not be predictable by the present model (eq 8). We believe this to be caused by the small pore radius of the VPI-5 material which is less than twice the t_f factor. It would, thus, be interesting to study materials with pore radii within the range of 6−10 Å to explore the range of validity of "Kelvin's law" and to understand in more detail the physics behind the t_f factor introduced in eq 8. For instance, the t_f factor is—in this work—assumed to be constant; however it might well be that t_f is a function of the pore radius R_p in much the same way as t_{ads} in N_2 adsorption is a function of R_p. Additional data (larger number of different pore size materials) are needed to undertaken such a study.

It is possible to derive an analytical function describing the pore size distribution dI/dR_p from the ^1H NMR IT curve by noting that

$$\frac{dI}{dR_p} = \frac{dI}{dX} \frac{dX}{dR_p} \tag{10}$$

and

$$\Delta T = T_0 - T = T_0 - \frac{10^3}{X} = \frac{K_f}{R_p + t_f} \tag{11}$$

By combining eqs 7, 10, and 11, the following formula is derived

$$\frac{dI}{dR_p} = \sum_{i=1}^{N} \frac{I_{0i}}{10^3 K_f \Delta_i \sqrt{2\pi}} (XT_0 - 10^3)^2 \exp\left(-\frac{X - X_{ci}}{\sqrt{2}\Delta_i}\right)^2 \tag{12}$$

All symbols are previously defined. The pore size distribution curves, dI/dR_p vs R_p (eq 12) derived from the ^1H NMR IT curves of samples 1−3 are displayed in Figure 11 and show that the shape of the curves are in agreement with the corresponding dV/dR_p curves obtained from N_2 adsorption (Figure 4). Moreover, consistency between pore radii determined by N_2 adsorption and HREM is found (Table 2).

To test the applicability of eq 12, the pore size distribution of a more complex pore system of amorphous silica was investigated by both N_2 adsorption and ^1H NMR. Equation 6 was fitted to the ^1H NMR IT curves and the fitted parameters (X_{ci}, I_{i0}, and Δ_i) were inserted into eq 12, from which dI/dR_p vs R_p (eq 12) was derived. The pore size distribution determined by N_2 adsorption is somewhat broader than the corresponding width of the distribution determined by ^1H NMR. Moreover, the pore size distribution, determined by N_2 adsorption, indicates a bimodal distribution with one distribution centered around 20

Å and the other around 28 Å. The pore size distribution determined by NMR could be improved by adding additional Gaussian functions to eq 6 before curve fitting; however, there is no statistical validity for such an approach due to the limited number of data points on the IT curve in the actual temperature range. These factors may account for the differences observed in the distributions determined by the two different techniques. However, qualitatively, the two distributions are rather similar.

The relative uncertainty in the determination of pore radius ($\sigma(R_p)/R_p$) from ^{1}H NMR can be estimated from eq 5

$$\frac{\sigma(R_p)}{R_p} = \frac{(R_p + t_f)^2}{R_p K_f}\, \sigma(\Delta T) \tag{13}$$

where $\sigma(\Delta T)$ is the uncertainty in the determined transition temperature T_c. Assuming $\sigma(\Delta T)$ to be ±0.5 °C, eq 13 predicts a relative uncertainty in R_p of less than 10% for $R_p < 200$ Å. For larger pore radii, the relative error in R_p increases approximately linearly with R_p. Thus, the present NMR technique is advantageous for pore radii less than approximately 500 Å (corresponding to a relative uncertainty in R_p of less than 25%) and larger than 10 Å. It must be emphasized that the use of liquids other than water will change the parameter K_f and thus also the relative uncertainty in the derived pore radii. A large K_f implies better sensitivity and a smaller uncertainty in R_p.

Conclusion

A combined use of ^{1}H NMR spectroscopy, N_2 adsorption, and HREM on MCM-41 mesoporous materials made it possible to establish a simple relation between the freezing point depression, ΔT, of confined pore water and the pore radius, R_p. The relation takes the form $\Delta T = K_f/(R_p - t_f)$, with t_f and K_f being constants. The t_f factor is tentatively proposed to be identical to the thickness of a nonfreezing pore surface water. Using the above equation, a mathematical model is derived which enables the pore size distribution to be determined from ^{1}H NMR intensity vs temperature measurements of water-saturated porous materials. This new method for the determination of pore size distributions of mesoporous materials ($R_p > 10$ Å) may be valuable to other investigators who are interested in these materials for potential applications within the fields of catalysis and separation. However, the application of this method to microporous materials ($R_p < 10$ Å) may be limited.